



27 **Abstract:** Millennial-scale East Asian monsoon variability is closely associated with natural
28 hazards through long-term variability in flood and drought cycles. Therefore, exploring what
29 drives the millennial-scale variability is of significant importance for future prediction of extreme
30 climates. Here we present a new East Asian summer monsoon (EASM) rainfall reconstruction
31 from the northwest Chinese loess plateau spanning the past 650 ka. The magnitude of
32 millennial-scale variability (MMV) in EASM rainfall is linked to ice volume and greenhouse gas
33 (GHG) at the 100-kyr earth-orbital eccentricity band and to GHG and summer insolation at the
34 precession band. At the glacial-interglacial cycle, gradual changes in CO₂ at times of intermediate
35 ice volume leads to increased variability in North Atlantic stratification and Atlantic meridional
36 overturning circulation, propagating abrupt climate changes into East Asia via the westerlies.
37 Within the 100-kyr cycle precession variability further enhances the response, showing that
38 stronger insolation and increased atmospheric GHG cause increases in the MMV of EASM
39 rainfall. These findings indicate increased extreme precipitation events under future warming
40 scenarios, consistent with model results.

41 **Key words:** EASM rainfall, MMV, GHG modulation, precession band

42

43 **1. Introduction**

44 Chinese loess is a unique terrestrial archive that can well document East Asian monsoon
45 (EAM) variability at tectonic to millennial timescales (Porter and An, 1995; An et al., 2011).
46 High-resolution loess records have revealed persistent millennial-scale (1-10 kyr periodicity)
47 EAM fluctuations spanning the last several glacial cycles (Guo et al., 1996; Sun et al., 2012,
48 2021a,b; Guo et al., 2021), which are dynamically linked with high-latitude abrupt changes in the



49 north Atlantic including Heinrich (H) (Heinrich, 1988) and Dansgaard-Oeschger (DO) events
50 (Dansgaard et al., 1982). This millennial-scale monsoon variability is superimposed on
51 glacial-interglacial variations (Ding et al., 1999; Clemens et al., 2018). Abrupt summer monsoon
52 changes are closely linked to natural hazards such as flood and drought events (Huang et al., 2007),
53 since the summer monsoon plays a leading role in transporting water vapor from low to
54 middle/high latitudes of the northern hemisphere (Liu et al., 2013; An et al., 2015). Abrupt rainfall
55 events associated with short-term summer monsoon variations strongly influence agriculture, food
56 production, water supply and social economic development (Huang et al., 2007; Cook et al., 2010;
57 Li et al., 2017). However, how these flood/drought events are affected by both natural and
58 anthropogenic factors remains poorly constrained. Understanding the mechanisms that modulate
59 the magnitude of millennial-scale variability (MMV) is of critical importance for the scientific
60 community as well as policy makers. Here we use the term “modulate” in the context of
61 lower-frequency components of the climate system influencing or determining the amplitude of a
62 higher-frequency components.

63 A number of well-dated, high-resolution speleothem $\delta^{18}\text{O}$ records have been developed in
64 recent years (Wang et al., 2008; Cheng et al., 2016), providing the opportunity to examine the
65 underlying relationship(s) between East Asian monsoon MMV and potential longer-term
66 (orbital-scale) modulators. The latest research suggests that the MMV through the Pleistocene is
67 influenced by both glacial boundary condition and orbital configurations (Sun et al., 2021b).
68 Cheng et al., (2016) hypothesized, on the basis of an East Asian composite speleothem $\delta^{18}\text{O}$
69 record ($\delta^{18}\text{O}_{\text{sp}}$), that periods of maximum Northern Hemisphere summer insolation correspond to
70 weaker millennial-scale variability. Subsequently, however, Thirumalai et al (2020) showed that



71 precession does not modulate the MMV of $\delta^{18}\text{O}_{\text{sp}}$ and postulated that it is, instead, modulated by
72 internal processes related to the cryosphere. This work also raised the possibility that $\delta^{18}\text{O}_{\text{sp}}$ is
73 decoupled from regional Asian monsoon rainfall over millennial timescales (Zhang et al., 2018).
74 As such, two important outstanding questions remain; is there a reliable proxy for East Asian
75 summer monsoon (EASM) rainfall at the millennial timescale and what factors modulate the
76 MMV thereof?

77 Due to weak pedogenesis and high sedimentation rates, millennial-scale oscillations are well
78 preserved in the western and northwestern Chinese Loess Plateau (CLP) over the past glacial
79 cycles (Sun et al., 2012, 2021a; Guo et al., 2021). The Linxia profile is well-suited for
80 reconstructing rapid monsoon changes because it is located in monsoon frontal zone and sensitive
81 to high- and low-latitude climate variability. To address the above questions, we have generated a
82 high-resolution summer monsoon proxy (Ca/Ti) from Linxia on the western CLP (Fig. 1). The
83 Ca/Ti ratio is a precipitation-sensitive proxy linked to summer monsoon rainfall (Guo et al., 2021).
84 Low values of Ca/Ti indicate stronger Ca leaching associated with intensified summer rainfall.
85 The new precipitation proxy (Ca/Ti) and $\delta^{18}\text{O}_{\text{sp}}$ are evaluated to elucidate the modulating drivers
86 of these two proxy records. As discussed in the Results section, we find that the MMV of Ca/Ti is
87 mainly modulated by ice volume and greenhouse gases (GHG) at the eccentricity band. Both
88 GHG and summer insolation modulate the MMV of Ca/Ti at the precession band but not that of
89 $\delta^{18}\text{O}_{\text{sp}}$; $\delta^{18}\text{O}_{\text{sp}}$ MMV is modulated by winter insolation at the eccentricity and obliquity bands.
90 The interpretations of these results are presented in the Discussion section.

91 **2. Materials and Methods**

92 The Linxia (LX; 103.63°E, 35.15°N, 2,200 m a.s.l.) loess record is from the western edge of the



93 CLP (Fig. 1). At present, mean annual temperature and precipitation in this region are about 8.1°C
94 and 484 mm, respectively, with ~80% of the annual precipitation falling during the summer season
95 (May to September). The 203.8 m-long core A (LXA) consists of 185 m of eolian loess-paleosol
96 sequences, underlain by 17 m of fluvial loess and 1.8 m of sandy gravel layers. The 72 m-long
97 core B (LXB) and a 7 m pit were excavated in 2017. Powder samples were collected at 2 cm
98 intervals for analyzing mean grain size (MGS). As well, 2-cm resolution samples were dried at
99 40°C overnight and ground to 200 mesh size (about <75 μm) with an agate mortar and pestle, and
100 then pressed into a plastic sheet (4 cm × 4 cm × 0.3 cm), creating a flat and homogeneous slide.
101 The plastic slides were then placed on a wood pallet for XRF scanning to obtain elemental
102 intensities (Guo et al., 2021).

103 The upper 18 m is mapped to the OSL-dated Yuanbao loess outcrop (~4 kilometers away) (Lai
104 et al., 2006). The chronostratigraphy has been generated using an independent loess chronology
105 generated by synchronizing Chinese loess and speleothem $\delta^{18}\text{O}$ records back to 650 ka (Sun et al.,
106 2021a). The first set of control points tie the loess/paleosol boundaries S_6 to S_0 to the timing of the
107 glacial terminations/inceptions in speleothem $\delta^{18}\text{O}$ (Cheng et al., 2016). The second and third sets
108 of age control points tie the timing of precessional transition boundaries and abrupt cooling events
109 in the MGS record to those in speleothem $\delta^{18}\text{O}$ (Fig. 2), based on the assumption that the East
110 Asian summer and winter monsoon co-vary with each other at orbital timescales, and
111 millennial-scale abrupt events are synchronous in the northern hemisphere (Hemming et al., 2004;
112 Sun et al., 2012; Clemens et al., 2018). The tie points are shown in Fig. 2.

113 In order to estimate the MMV, all the raw datasets are linear interpolated at 0.1 kyr interval. The
114 original time series are filtered using a Butterworth filter at a cutoff threshold of 10 kyr (e.g.



115 Ca/Ti-hi-10kyr). The moving standard deviation of millennial-scale variability is calculated to
116 ascertain the orbitally-related modulation and its association with internal and external forcing
117 using 2 kyr sliding window (calculation method follows Thirumalai et al., 2020). The spectra of
118 all proxies were calculated using the Lomb-Scargle periodogram
119 (<https://exoplanetarchive.ipac.caltech.edu/cgi-bin/Pgram/nph-pgram>), which has the advantage of
120 analyzing discontinuous time series and removal of spurious spectral characteristics (VanderPlas,
121 2018). Normalized and combined orbital parameters eccentricity, tilt, and negative precession
122 (ETP), GHG, insolation, and benthic $\delta^{18}\text{O}$ were evaluated by wavelet coherence (WTC) to extract
123 maximal phase and amplitude correlations with astronomical, ice volume and greenhouse gases
124 forcing over the past 650 ka. WTC between time series was performed in a Monte Carlo
125 framework ($n = 1,000$) following Grinsted et al., (2004). The WTC would help to detect the
126 period in different frequency bands where the two time series co-vary (but does not necessarily
127 have high power). The black arrows in the figures represent the phase relationship between the
128 two time sequences with rightward, upward and downward arrows indicate the in-phase, leading
129 and lagging phase, respectively. The colour scale indicates the amplitude correlations between the
130 two datasets.

131 In this paper, the parameter $\Delta\text{RF}_{\text{GHG}}$ is regarded as GHG radiative forcing (GHG RF, using the
132 GHG RF instead of $\Delta\text{RF}_{\text{GHG}}$ in the discussion section) and applied in WTC to evaluate the
133 relationship between MMV of Ca/Ti and $\delta^{18}\text{O}$ sp. The $\Delta\text{RF}_{\text{GHG}}$ is reconstructed by referencing the
134 content of EPICA ice core greenhouse gases to the modern value.

135 $\Delta\text{RF}_{\text{GHG}}$ is defined as the difference between a certain past GHG level ($[\text{CO}_2]$ and $[\text{CH}_4]$) and the
136 pre-industrial greenhouse gas level ($[\text{CO}_2]_0 = 280$ ppm, $[\text{CH}_4]_0 = 700$ ppb) (Ramaswamy et al.,



137 2001). While CH₄ contributes <5%, we calculated the $\Delta\text{RF}_{\text{GHG}}$ using both CO₂ and CH₄. The
138 equation used to determine $\Delta\text{RF}_{\text{GHG}}$ is as follows (Lo et al., 2017):

$$\begin{aligned} 139 \quad \Delta\text{RF}_{\text{GHG}} &= \Delta\text{RF}_{\text{CO}_2} + \Delta\text{RF}_{\text{CH}_4} \\ 140 \quad &= 4.841 \ln\left(\frac{[\text{CO}_2]}{[\text{CO}_2]_0}\right) + 0.0906\left(\sqrt{[\text{CO}_2]} - \sqrt{[\text{CO}_2]_0}\right) + 0.036 \ln\left(\frac{[\text{CH}_4]}{[\text{CH}_4]_0}\right) \end{aligned}$$

141 3. Results

142 The MGS reflects grain-size sorting and is very sensitive to winter monsoon variations (Porter
143 and An, 1995; Sun et al., 2006) with larger particle size during the glacial. The Ca/Ti ratio
144 reflects precipitation-induced leaching intensity linked to summer monsoon rainfall (Guo et al.,
145 2021), with lower value during the interglacials. The high resolution $\delta^{18}\text{O}$ of Sanbao-Hulu
146 speleothem is an indicator of EASM changes at orbital to centennial timescales (Cheng et al.,
147 2016). The MGS and Ca/Ti exhibit distinct glacial-interglacial and precessional variations over the
148 last 650 ka as seen in LR04 $\delta^{18}\text{O}$ (Lisiecki and Raymo, 2005) and speleothem $\delta^{18}\text{O}$ (Cheng et al.,
149 2016), respectively (Fig. 2).

150 Both Ca/Ti and $\delta^{18}\text{O}_{\text{sp}}$ records show clear millennial-scale fluctuations overlaying orbital-scale
151 variations. The high frequency millennial signals (Materials and Methods) persist over the last 650
152 ka, but the amplitude varies from proxy to proxy (Fig. 3a and S1a). Spectral analysis of the raw
153 records and MMV for loess and speleothem records display variable associations with
154 eccentricity- (~100 kyr), obliquity- (~41 kyr), and precession-scale (~23 and ~19 kyr) over the
155 past 650 ka. Loess Ca/Ti variance is mainly concentrated in obliquity with lesser variance in the
156 eccentricity and precession bands (Fig. 3b), indicating prominent ice volume (eccentricity and
157 obliquity) and isolation (precession) forcing. The speleothem $\delta^{18}\text{O}$ shows predominant
158 precession-scale variance (Fig. S1b) suggesting strong links to insolation forcing (Cheng et al.,



159 2016). These results indicate ice volume and insolation play dominant roles in driving changes in
160 loess Ca/Ti and speleothem $\delta^{18}\text{O}$, respectively (Cheng et al., 2016; Sun et al., 2021a).

161 Millennial-scale fluctuations co-exist with long-term orbital- and ice-volume variability; we
162 seek to assess the potential linkages among them and in particular, the extent to which MMV is
163 modulated by these longer-term orbital and internal climate parameters. The spectra of Ca/Ti
164 MMV shows dominant eccentricity with less strong precession and weak obliquity variance (Fig.
165 3d). The spectrum of $\delta^{18}\text{Osp}$ MMV has a small peak near 100 kyr and an offset 41 kyr peak with
166 little to no variance at the 23 kyr period (Fig. S1d). Thus, while both proxies are similarly
167 modulated at the 100-kyr period (such that the MMV is larger during glacial intervals relative to
168 interglacial times) the MMV modulation is variable for the two proxies at other orbital bands.

169 As with the spectral differences in the raw records, the MMV spectra also implies different
170 MMV modulating drivers, potentially associations with insolation, ice volume, and/or GHG
171 (Thirumalai et al., 2020). How do internal and external drivers interact with each other and
172 modulate the MMV of these records at the orbital timescale? We performed wavelet coherence
173 and phase analyses of both MMV records relative to ETP, ice volume, $\Delta\text{RF}_{\text{GHG}}$, summer insolation,
174 and winter insolation to identify which variables might modulate the MMV of these EASM
175 records. The MMV in Ca/Ti is strongly coherent with ice volume and GHG at the 100,000-year
176 earth-orbital eccentricity band and with GHG and summer insolation at the 23,000-year precession
177 band (Figure 4c, d, g). $\delta^{18}\text{Osp}$ MMV is most strongly coherent with GHG and ice volume at the
178 100-kyr band and with winter insolation at the eccentricity and obliquity bands (Figure S2c, d, g).

179 **4. Discussion**

180 **4.1 Orbital-scale modulation factors for MMV of the EASM**



181 Previous geological records and modeling indicate that high latitude ice volume or ice sheet
182 topography play important roles in triggering abrupt climate changes (Broecker et al.,1994; Clark
183 et al., 2001). In particular, abrupt climate changes are highly sensitive to ice volume variations; ice
184 sheets are widely hypothesized to motivate and amplify these high frequency signals within a
185 constrained benthic oxygen isotope-“ice volume threshold” between 3.5 and 4.5‰ (Bailey et al.,
186 2010; Naffs et al., 2013; Zhang et al., 2014). Wavelet coherence between the MMV of loess Ca/Ti,
187 speleothem $\delta^{18}\text{O}$ and the global benthic $\delta^{18}\text{O}$ stack show excellent coherence and near-zero phase
188 with ice volume at the 100 kyr band (Fig. 4e, g and S2e, g); this in-phase variation demonstrates
189 that EASM MMV primarily follows the glacial-interglacial rhythm of ice volume variations,
190 enlarged during glacial times and dampened during interglacial times. However, coherence of the
191 MMV for these two proxies with the benthic $\delta^{18}\text{O}$ stack is relatively weak and variable at the 41
192 kyr band ($\delta^{18}\text{O}_{\text{sp}}$; Figure S2e, g) and 23-kyr band (Ca/Ti; Fig. 4e, g). These relationships
193 demonstrate that ice volume directly modulates the MMV of the EASM, predominantly at the 100
194 kyr band, with high ice volume corresponding to larger MMV.

195 GHG concentration is another potential driver of abrupt climate changes (Alvarez-Solas et al.,
196 2011; Zhang et al., 2017).Wavelet coherence between the MMV of loess Ca/Ti, speleothem $\delta^{18}\text{O}$
197 and the record of GHG RF show excellent coherence and $\sim 180^\circ$ phase at the 100-kyr eccentricity
198 band (Fig. 4b, d and Fig. S2b, d) indicating strong MMV at times of low GHG. Given the coupled
199 nature of global ice-volume and atmospheric GHG, it is clear that over the late Pleistocene
200 glacial-interglacial cycles, these two factors modulate the MMV of the EASM as recorded by
201 Ca/Ti and speleothem $\delta^{18}\text{O}$ such that abrupt climate change is amplified during times of high ice
202 volume and low GHG concentration. However, this is not the case for the precession band. MMV



203 of loess Ca/Ti displays discrete intervals high coherence and near-zero phase with GHG RF at the
204 precession band (Figure 4b, d), which is not the case for speleothem $\delta^{18}\text{O}$ (Figure S2b, d). Thus,
205 GHG RF does play a role in modulating Ca/Ti MMV but not that of $\delta^{18}\text{O}$ sp at the precession band,
206 indicating a difference in the millennial-scale response of these two proxies at this time-scale. We
207 investigate this further by assessing the response to local insolation forcing.

208 The MMV of Ca/Ti show discontinuous relatively weak coherence with 35°N summer
209 insolation at the precession band with even weaker coherence at the 41-kyr band (Figure 4a, c);
210 we note that the summer insolation modulation is less strong relative to that of GHG at the
211 precession band (Figure 4b, d). In contrast, the MMV of $\delta^{18}\text{O}$ sp displays high coherence and zero
212 phase with 35°N winter insolation at 100 kyr period, relatively weaker coherence, with a lagging
213 phase, at the 41 kyr band, and negligible coherence at the 23-ky band (Figure S2a, c). These
214 results indicate that the MMV of speleothem $\delta^{18}\text{O}$ is modulated by local winter insolation,
215 opposite to the Cheng et al., (2016) hypothesis calling on north hemisphere summer insolation.

216 **4.2 Mechanism and implication for modulation of EASM MMV**

217 At the glacial-interglacial timescale, the MMV is amplified under the glacial boundary
218 conditions. This indicates dynamic linkages with high latitude North Atlantic Heinrich and DO
219 events (Cheng et al., 2016; Sun et al., 2012, 2021a, b). Heinrich and DO variability are linked to
220 Northern Hemisphere ice sheet (NHIS) perturbations via its influence on fresh-water flux into the
221 North Atlantic Ocean and consequent Atlantic meridional overturning circulation (AMOC)
222 changes (McManus et al., 1999; Hemming, 2004; Naffs et al., 2013). At times of intermediate ice
223 sheet volume, minor changes in NHIS height and atmospheric CO_2 concentrations can trigger the
224 rapid climate transitions (Zhang et al., 2014, 2017). Altering the height of NHIS leads to changes



225 in the gyre circulation and sea-ice coverage by shifting the northern westerlies (Zhang et al., 2014).
226 The maximum westerly wind stress shifts northwards associated with gradual increase of the
227 Northern Hemisphere ice volume. The northward westerly, in turn, encourages the EASM rain
228 belt to move northward (He et al., 2021) and results in increases in the MMV of EASM rainfall
229 (especially northern China). In addition, CO₂ acts as an internal feedback agent to AMOC changes
230 (Barker et al., 2016). Under intermediate glacial condition, when the AMOC reaches a regime of
231 bi-stability, rising CO₂ during Heinrich Stadial cold events can trigger abrupt transitions to warm
232 conditions. Decreasing CO₂ during warm events leads to abrupt cooling transitions (Zhang et al.,
233 2017). Therefore, CO₂ generally provides a negative feedback on MMV of EASM rainfall. During
234 interglacial times decreasing ice volume, accompanied by reduced sea ice and more frequent
235 freshwater perturbation, is correlated with lower frequency and smaller amplitude variability in
236 abrupt climate events. The co-evolving GHG concentrations would further alter the sea surface
237 temperature by greenhouse forcing, subsequently modulating the MMV.

238 Within the 100,000-year cycle, precession-band variability (4-5 cycles), characterized by
239 increased insolation and atmospheric GHG, further heightens the positive response, leading to
240 larger MMV of subtropical rainfall. Recent transient sensitivity experiments suggests that
241 millennial-scale rainfall variability is driven primarily by meltwater and secondarily by insolation
242 (He et al., 2021). During interglacial times under the combined influence of insolation and CO₂,
243 model simulation shows that when insolation reaches the lower “threshold” value (between 358.2
244 and 352.1 W. m⁻²), it triggers a strong abrupt weakening of the AMOC and results in abrupt
245 cooling transitions over last 800 ka (Yin et al., 2021). Increased insolation could warm sea surface
246 temperature and accelerate freshwater input from high latitude ice sheet as well as altering GHG



247 concentration in the atmosphere (Lewkowicz and Way, 2019), which could, in turn, modulate
248 MMV changes in the low latitude monsoon regions.

249 If both millennial-scale Ca/Ti and $\delta^{18}\text{Osp}$ represent subtropical rainfall amount, the
250 modulation factors should be consistent. However, eccentricity, obliquity and precession bands
251 MMV modulators differ for loess Ca/Ti and $\delta^{18}\text{Osp}$, indicating they monitor different aspects of
252 millennial-scale monsoon circulations. Modern observations and Lagrangian trajectories of air
253 parcels in China during the summer monsoon indicate that moisture-induced precipitation doesn't
254 derive from the strongest water vapor pathways (Sun et al., 2011; Jiang et al., 2017); local water
255 vapor recycling contributes significantly to regional precipitation in East China (over 30%) and
256 North China (exceeding 55%) (Shi et al., 2020). Hence, we speculate that $\delta^{18}\text{Osp}$ MMV monitors
257 changes in the isotopic composition of rainfall, varying with changes in westerly transport paths
258 associated with North Atlantic cooling events, consistent with the MMV of $\delta^{18}\text{Osp}$ being closely
259 linked to winter insolation at 100- and 41- kyr periods and the absence of MMV modulation at
260 precession band. We further hypothesize that Ca/Ti mainly represents the MMV in local rainfall
261 amount, consistent with the MMV of tropical rainfall being more dynamically related to GHG and
262 summer insolation at precession band.

263 In recent decades atmospheric GHG concentration is accelerating due to anthropogenic
264 contribution of fossil fuels, suggesting that EASM (extreme) precipitation will increase as well.
265 This inference is consistent with model simulations indicating that the number of extreme daily
266 precipitation events and mean precipitation overall will increase significantly in response to higher
267 GHG concentration (Dairaku and Emori, 2006). The anthropogenic GHG-evoked warming is
268 projected to increase the lower-tropospheric water vapor content and enhance the thermal contrast



269 between land and ocean (Kitoh et al., 1997). This will give rise to a northward shift of lower
270 tropospheric monsoon circulation and an increase rainfall during the East Asian summer monsoon
271 (Vecchi and Soden, 2007). Our results indicate that factors modulating EASM precipitation MMV
272 in the past are consistent with those predicted to influence future changes in monsoonal
273 precipitation, lending further confidence in those projections.

274 **5. Conclusions**

275 Our high-resolution loess Ca/Ti record displays millennial monsoon oscillations that persist
276 over the last 650 ka. Wavelet results highlight remarkable GHG modulation at both 100 kyr and
277 precession band as well as ice volume at 100 kyr period and local insolation forcing at precession
278 band. The MMV of loess Ca/Ti and speleothem $\delta^{18}\text{O}$ are modulated by different orbital factors,
279 implying that these two proxies document different climatic response of millennial-scale monsoon
280 circulation. The inferred mechanism of how these internal and external factors modulate the MMV
281 calls on dynamic linkages to variability in AMOC at both eccentricity and precession bands. In
282 recent decades, atmospheric GHG concentration is dramatically increasing due to anthropogenic
283 contribution of fossil fuels (Bousquet et al., 2006; Davis et al., 2010), resulting in accelerated
284 melting of ice-sheets in bi-polar regions (Swingedouw et al., 2008; Golledge et al., 2019). Their
285 combined effects lead to more frequent occurrences of extreme rainfall (Dairaku and Emori, 2006;
286 IPCC, 2018). Our results indicate that the MMV EASM rainfall is modulated by ice volume, GHG,
287 and insolation factors, consistent with those predicted to influence future changes in monsoonal
288 precipitation.

289

290 **CRedit authorship contribution statement**



291 Fei Guo mainly contributes to the experiments, data analysis, idea and draft paper. Prof.
292 Steven Clemens and Youbin Sun help to design the program and revise the draft. Huimin Fan
293 assists to perform the experiments and data processing. Ting Wang, Yuming Liu and Xingxing Liu
294 make contributions to the fieldwork and paper discussion.

295

296 **Acknowledgments**

297 We thank Xiaojing Du for offering idea on potential model test for this paper. This work was
298 supported by grants from the Strategic Leading Research Program of Chinese Academy of Science
299 (XDB40000000) and National Natural Science Foundation of China (41525008 and 41977173).

300

301 **Declaration of Competing Interest**

302 The authors declare that they have no known competing financial interests or personal
303 relationships that could have appeared to influence the work reported in this paper.

304

305 **References**

- 306 Alvarez-Solas, J., Charbit, S., Ramstein, G., Paillard, D., Dumas, C., Ritz, C., and Roche, D. M.:
307 Millennial-scale oscillations in the Southern Ocean in response to atmospheric CO₂ increase,
308 *Global Planet. Change*, 76, 128-136, <https://doi.org/10.1016/j.gloplacha.2010.12.004>, 2011.
- 309 An, Z., Clemens, S. C., Shen, J., Qiang, X., Jin, Z., Sun, Y., Prell, W. L., Luo, J., Wang, S., Xu, H.,
310 Cai, Y., Zhou, W., Liu, X., Liu, W., Shi, Z., Yan, L., Xiao, X., Chang, H., Wu, F., Ai, L., and Lu,
311 F.: Glacial-interglacial Indian summer monsoon dynamics, *Science*, 333, 719-723,
312 <https://doi.org/10.1126/science.1203752>, 2011.
- 313 An, Z., Wu, G., Li, L., Li, J., Sun, Y., Liu, Y., Zhou, W., Cai, Y., Duan, A., Li, L., Mao, J., Cheng,
314 H., Shi, Z., Tan, L., Yan, H., Ao, H., Chang, H., and Feng, J.: Global monsoon dynamics and
315 climate change, *Annu. Rev. Earth Planet.*, 43, 29-77,
316 <https://doi.org/10.1146/annurev-earth-060313-054623>, 2015.



- 317 Bailey, I., Bolton, C. T., DeConto, R. M., Pollard, D., Schiebel, R., and Wilson, P. A.: A low
318 threshold for North Atlantic ice rafting from “low-slung slippery” late Pliocene ice sheets,
319 *Paleoceanography*, 25, PA1212, <https://doi.org/10.1029/2009PA001736>, 2010.
- 320 Barker, S., and Knorr, G.: A paleo-perspective on the AMOC as a tipping element, *PAGES News*,
321 24, 14-15, <http://orca.cardiff.ac.uk/id/eprint/95186>, 2016.
- 322 Bousquet, P., Ciais, P., Miller, J. B., Dlugokencky, E. J., Hauglustaine, D. A., Prigent, C., and
323 White, J.: Contribution of anthropogenic and natural sources to atmospheric methane variability,
324 *Nature*, 443, 439-443, <https://doi.org/10.1038/nature05132>, 2006.
- 325 Broecker, W. S.: Massive iceberg discharges as triggers for global climate change, *Nature*, 372
326 421-424, <https://doi.org/10.1038/372421a0>, 1994.
- 327 Cheng, H., Edwards, L., Sinha, A., Spötl, C., Yi, L., Chen, S., Kelly, M., Kathayat, G., Wang, X. F.,
328 Li, X. L., Kong, X. G., Wang, Y. J., Ning, Y.F., and Zhang, H. W.: The Asian monsoon over the
329 past 640,000 years and ice age terminations, *Nature*, 534, 640-646,
330 <https://doi.org/10.1038/nature18591>, 2016.
- 331 Clark, P. U., Marshall, S. J., Clarke, G. K., Hostetler, S. W., Licciardi, J. M., and Teller, J. T.:
332 Freshwater forcing of abrupt climate change during the last glaciation, *Science*, 293, 283-287,
333 <https://doi.org/10.1126/science.1062517>, 2001.
- 334 Clemens, S. C., Holbourn, A., Kubota, Y., Lee, K. E., Liu, Z., Chen, G., Nelson, A., and
335 Fox-Kemper, B.: Precession-band variance missing from East Asian monsoon runoff, *Nat.*
336 *Commun.*, 9, 1-12, <https://doi.org/10.1038/s41467-018-05814-0>, 2018.
- 337 Cook, E. R., Anchukaitis, K. J., Buckley, B. M., D’Arrigo, R. D., Jacoby, G. C., and Wright, W. E.:
338 Asian monsoon failure and megadrought during the last millennium, *Science*, 328, 486-489,
339 <https://doi.org/10.1126/science.1185188>, 2010.
- 340 Dansgaard, W., Clausen, H. B., Gundestrup, N., Hammer, C. U., Johnsen, S. F., Kristinsdottir, P.
341 M., and Reeh, N.: A new Greenland deep ice core, *Science*, 218, 1273-1277,
342 <https://doi.org/10.1126/science.218.4579.1273>, 1982.
- 343 Dairaku, K., and Emori, S.: Dynamic and thermodynamic influences on intensified daily rainfall
344 during the Asian summer monsoon under doubled atmospheric CO₂ conditions, *Geophys. Res.*
345 *Lett.*, 33, L01704, <https://doi.org/10.1029/2005GL024754>, 2006.



- 346 Davis, S. J., Caldeira, K., and Matthews, H. D.: Future CO₂ emissions and climate change from
347 existing energy infrastructure, *Science*, 329, 1330-1333,
348 <https://doi.org/10.1126/science.1188566>, 2010.
- 349 Golledge, N. R., Keller, E. D., Gomez, N., Naughten, K. A., Bernales, J., Trusel, L. D., and
350 Edwards, T. L.: Global environmental consequences of twenty-first-century ice-sheet melt,
351 *Nature*, 566, 65-72, <https://doi.org/10.1038/s41586-019-0889-9>, 2019.
- 352 Grinsted, A., Moore, J. C., and Jevrejeva, S.: Application of the cross wavelet transform and
353 wavelet coherence to geophysical time series, *Nonlinear Proc. Geoph.*, 11, 561-566,
354 <https://doi.org/10.5194/npg-11-561-2004>, 2004.
- 355 Guo, F., Clemens, S. C., Wang, T., Wang, Y., Liu, Y., Wu, F., Jin, Z., and Sun, Y.: Monsoon
356 variations inferred from high-resolution geochemical records of the Linxia loess/paleosol
357 sequence, western Chinese Loess Plateau, *Catena*, 198, 105019,
358 <https://doi.org/10.1016/j.catena.2020.105019>, 2021.
- 359 Guo, Z., Liu, T., Guiot, J., Wu, N., Lü, H., Han, J., and Gu, Z.: High frequency pulses of East
360 Asian monsoon climate in the last two glaciations: link with the North Atlantic. *Clim. Dynam*,
361 12, 701-709, <https://doi.org/10.1007/s003820050137>, 1996.
- 362 He, C., Liu, Z., Otto-Bliesner, B. L., Brady, E. C., Zhu, C., Tomas, R., Clark, P. U., Zhu, J., Jahn,
363 A., Gu, S., and Zhang, J., Nusbaumer, J., Noone, D., Cheng, H., Wang, Y., Yan, M., and Bao, Y.:
364 Hydroclimate footprint of pan-Asian monsoon water isotope during the last deglaciation, *Sci.*
365 *Adv.*, 7, eabe2611, <https://doi.org/10.1126/sciadv.abe2611>, 2021.
- 366 Heinrich, H.: Origin and consequences of cyclic ice rafting in the northeast Atlantic Ocean during
367 the past 130,000 years, *Quat. Res.*, 29, 142-152, [https://doi.org/10.1016/0033-5894\(88\)90057-9](https://doi.org/10.1016/0033-5894(88)90057-9),
368 1988.
- 369 Hemming, S. R.: Heinrich events: Massive late Pleistocene detritus layers of the North Atlantic
370 and their global climate imprint, *Rev. Geophys.*, 42, RG1005,
371 <https://doi.org/10.1029/2003RG000128>, 2004.
- 372 Hoegh-Guldberg, O., Jacob, D., and Bindi, M., et al.: Impacts of 1.5 C global warming on natural
373 and human systems. Global warming of 1.5 C, An IPCC Special Report. IPCC Secretariat,
374 175-311, <http://hdl.handle.net/10138/311749>, 2018.



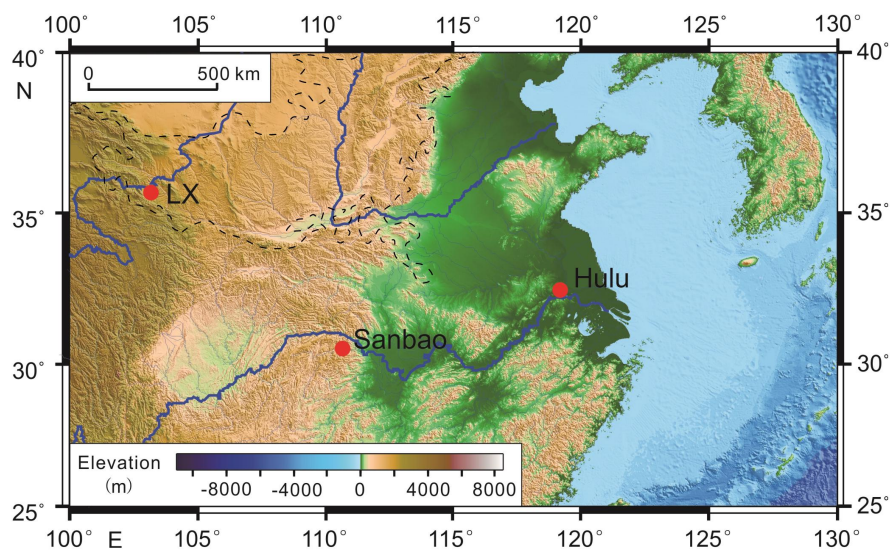
- 375 Huang, R., Chen, J., and Huang, G.: Characteristics and variations of the East Asian monsoon
376 system and its impacts on climate disasters in China, *Adv. Atmos. Sci.*, 24, 993-1023,
377 <https://doi.org/10.1007/s00376-007-0993-x>, 2007.
- 378 Jiang, Z., Jiang, S., Shi, Y., Liu, Z., Li, W., and Li, L.: Impact of moisture source variation on
379 decadal-scale changes of precipitation in North China from 1951 to 2010, *Geophys. Res.*
380 *Atmos.*, 122, 600-613, <https://doi.org/10.1002/2016JD025795>, 2017.
- 381 Kitoh, A., Yukimoto, S., Noda, A., and Motoi, T.: Simulated changes in the Asian summer
382 monsoon at times of increased atmospheric CO₂, *J. Meteorol. Soc. JPN. Ser. II*, 75, 1019-1031,
383 https://doi.org/10.2151/jmsj1965.75.6_1019, 1997.
- 384 Lai, Z. P., and Wintle, A. G.: Locating the boundary between the Pleistocene and the Holocene in
385 Chinese loess using luminescence, *Holocene* 16, 893-899,
386 <https://doi.org/10.1191/0959683606hol980rr>, 2006.
- 387 Lewkowicz, A. G., and Way, R. G.: Extremes of summer climate trigger thousands of thermokarst
388 landslides in a High Arctic environment, *Nat. Commun.*, 10, 1-11,
389 <https://doi.org/10.1038/s41467-019-09314-7>, 2019.
- 390 Lisiecki, L. E., and Raymo, M. E.: A Pliocene-Pleistocene stack of 57 globally distributed benthic
391 $\delta^{18}\text{O}$ records, *Paleoceanography*, 20, PA1003, <https://doi.org/10.1029/2004PA001071>, 2005.
- 392 Liu, J., Wang, B., Cane, M. A., Yim, S. Y., and Lee, J. Y.: Divergent global precipitation changes
393 induced by natural versus anthropogenic forcing, *Nature*, 493, 656-659,
394 <https://doi.org/10.1038/nature11784>, 2013.
- 395 Lo, L., Chang, S. P., Wei, K. Y., Lee, S. Y., Ou, T. H., and Chen, Y. C., et al.: Nonlinear climatic
396 sensitivity to greenhouse gases over past 4 glacial/interglacial cycles, *Sci. Rep.*, 7, 1-7,
397 <https://doi.org/10.1038/s41598-017-04031-x>, 2017.
- 398 McManus, J. F., Oppo, D. W., and Cullen, J. L.: A 0.5-million-year record of millennial-scale
399 climate variability in the North Atlantic, *Science*, 283, 971-975,
400 <https://doi.org/10.1126/science.283.5404.971>, 1999.
- 401 Naafs, B. D. A., Hefter, J., and Stein, R.: Millennial-scale ice rafting events and Hudson Strait
402 Heinrich (-like) Events during the late Pliocene and Pleistocene: a review, *Quat. Sci. Rev.*, 80,
403 1-28, <https://doi.org/10.1016/j.quascirev.2013.08.014>, 2013.



- 404 Porter, S. C., and An Z. S.: Correlation between climate events in the North Atlantic and China
405 during the last glaciation, *Nature*, 375, 305-308, <https://doi.org/10.1038/375305a0>, 1995.
- 406 Ramaswamy, V. et al.: Radiative forcing of climate change in *Climate Change 2001: The*
407 *Scientific Basis*, Cambridge University Press, 349-416,
408 <https://csl.noaa.gov/assessments/ozone/1991/chapters/chapter7.pdf>, 2001.
- 409 Shi, Y., Jiang, Z., Liu, Z., and Li, L.: A Lagrangian analysis of water vapor sources and pathways
410 for precipitation in East China in different stages of the East Asian summer monsoon, *J. Clim.*,
411 33, 977-992, <https://doi.org/10.1175/JCLI-D-19-0089.1>, 2020.
- 412 Sun, B., Zhu, Y., and Wang, H.: The recent interdecadal and interannual variation of water vapor
413 transport over eastern China, *Adv. Atmos. Sci.*, 28, 1039-1048,
414 <https://doi.org/10.1007/s00376-010-0093-1>, 2011.
- 415 Sun, Y., Clemens, S. C., An, Z., and Yu, Z.: Astronomical timescale and palaeoclimatic implication
416 of stacked 3.6-Myr monsoon records from the Chinese Loess Plateau, *Quat. Sci. Rev.*, 25, 33-48.
417 <https://doi.org/10.1016/j.quascirev.2005.07.005>, 2006.
- 418 Sun, Y., Clemens, S., Guo, F., Liu, X., Wang, Y., Yan, Y., and Liang, L.: High-sedimentation-rate
419 loess records: A new window into understanding orbital-and millennial-scale monsoon
420 variability, *Earth-Sci. Rev.*, 103731, <https://doi.org/10.1016/j.earscirev.2021.103731>, 2021a.
- 421 Sun, Y., Clemens, S. C., Morrill, C., Lin, X., Wang, X., and An, Z.: Influence of Atlantic
422 meridional overturning circulation on the East Asian winter monsoon, *Nat. Geosci.*, 5, 46-49,
423 <https://doi.org/10.1038/ngeo1326>, 2012.
- 424 Sun, Y., McManus, J. F., Clemens, S. C., Zhang, X., Vogel, H., Hodell, D. A., Guo, F., Wang, T.,
425 Liu, X., and An, Z.: Persistent orbital influence on millennial climate variability through the
426 Pleistocene, *Nat. Geosci.*, 14, 812-818, <https://doi.org/10.1038/s41561-021-00794-1>, 2021b.
- 427 Swingedouw, D., Fichefet, T., Huybrechts, P., Goosse, H., Driesschaert, E., and Loutre, M. F.:
428 Antarctic ice-sheet melting provides negative feedbacks on future climate warming, *Geophys.*
429 *Res. Lett.*, 35, <https://doi.org/10.1029/2008GL034410>, 2008.
- 430 Thirumalai, K., Clemens, S. C., and Partin, J. W.: Methane, Monsoons, and Modulation of
431 Millennial-Scale Climate, *Geophys. Res. Lett.*, 47, e2020GL087613,
432 <https://doi.org/10.1029/2020GL087613>, 2020.



- 433 Vecchi, G. A., and Soden, B. J.: Global warming and the weakening of the tropical circulation, J.
434 Clim., 20, 4316-4340, <https://doi.org/10.1175/JCLI4258.1>, 2007.
- 435 VanderPlas, J. T.: Understanding the lomb-scargle periodogram, The Astrophysical Journal
436 Supplement Series, 236, 16, <https://doi.org/10.3847/1538-4365/aab766>, 2018.
- 437 Wang, Y., Cheng, H., Edwards, R. L., Kong, X., Shao, X., Chen, S., and An, Z. Millennial-and
438 orbital-scale changes in the East Asian monsoon over the past 224,000 years, Nature, 451,
439 1090-1093, <https://doi.org/10.1038/nature06692>, 2008.
- 440 Yin, Q. Z., Wu, Z. P., Berger, A., Goosse, H., Hodell, D.: Insolation triggered abrupt weakening of
441 Atlantic circulation at the end of interglacials, Science, 373, 1035-1040,
442 <https://doi.org/10.1126/science.abg1737>, 2021.
- 443 Zhang, H., Griffiths, M. L., Chiang, J.C.H., Kong, W., Wu, S., Atwood, A., Huang, J., Cheng, H.,
444 Ning, Y., and Xie, S.: East Asian hydroclimate modulated by the position of the westerlies
445 during Termination I, Science, 362, 580-583, <https://doi.org/10.1126/science.aat9393>, 2018.
- 446 Zhang, X., Knorr, G., Lohmann, G., and Barker, S.: Abrupt North Atlantic circulation changes in
447 response to gradual CO₂ forcing in a glacial climate state, Nat. Geosci., 10, 518-523,
448 <https://doi.org/10.1038/ngeo2974>, 2017.
- 449 Zhang, X., Lohmann, G., Knorr, G., and Purcell, C.: Abrupt glacial climate shifts controlled by ice
450 sheet changes, Nature, 512, 290-294, <https://doi.org/10.1038/nature13592>, 2014.
- 451



452

453

454

455

456

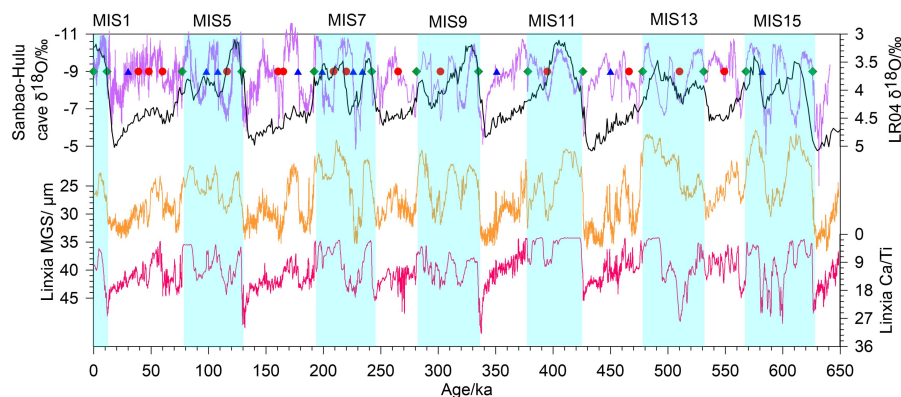
457

458

459

460

Figure. 1 The location of the Linxia (LX) loess profile and Hulu-Sanbao cave records. The Linxia profile, located on the edge of convergence zone for of alpine Qinghai-Tibet Plateau, northwest arid and the southeast monsoon area, is very sensitive to the migration of desert regions and monsoonal rainfall. Sanbao-Hulu cave is located in monsoon-influenced Yangtze River Valley, sensitive to the monsoon-induced precipitation changes. Black dash line represents the scope of Chinese Loess Plateau. The base map is drawn using GMT software, and the elevation data is from <http://www.ngdc.noaa.gov/mgg/global/global.html>.



461

462

Figure 2 Variations of mean grain size, Ca/Ti over last 650 ka and age model of Linxia loess

463

section. Comparison of mean grain size and Ca/Ti in Linxia section with Sanbao-Hulu (Cheng et

464

al., 2009, 2016) and benthic $\delta^{18}\text{O}$ stack (Lisiecki and Raymo, 2005). The dark brown squares, blue

465

triangles and red dots represent the first (glacial-interglacial transition), second (precession cycles)

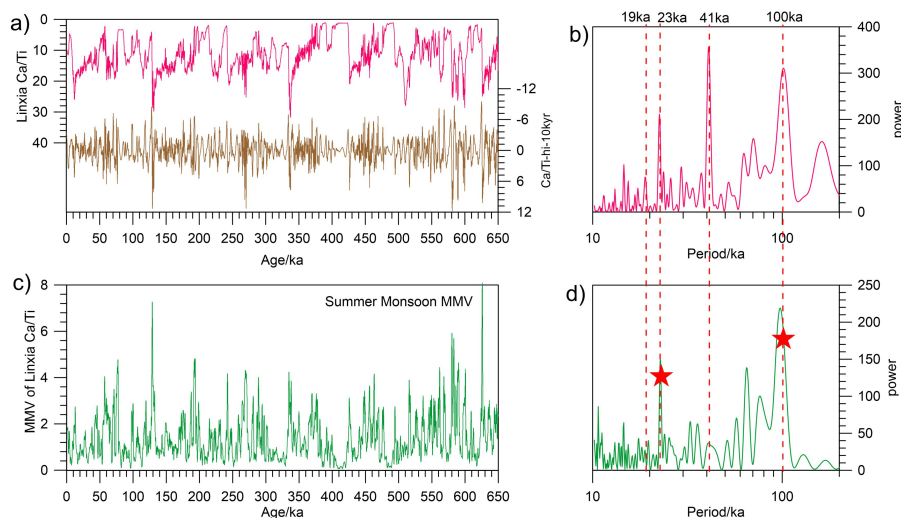
466

and third (millennial-scale events) class age control points at the corresponding position of cave

467

record, respectively (Sun et al., 2021a). Light blue bands donate the interglacial times.

468



469

470

471

472

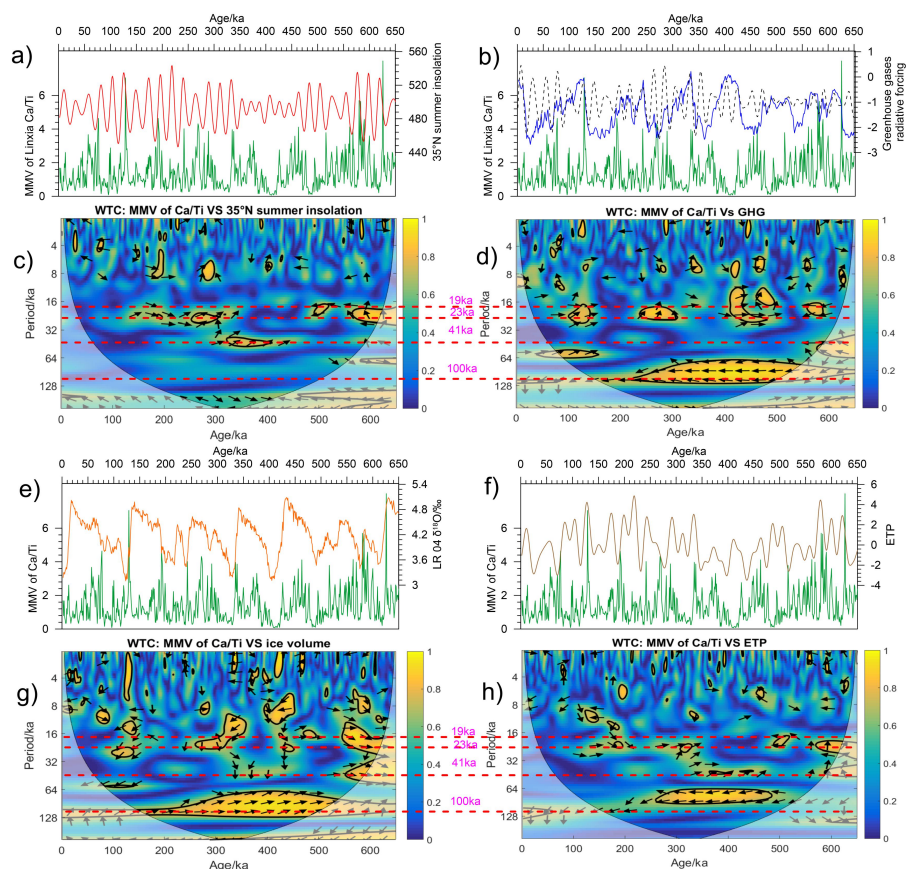
473

474

475

476

Figure. 3 Raw datasets, millennial-scale components (10 kyr high pass filtering signals) and MMV of the Linxia loess Ca/Ti record over the past 650 ka with their corresponding spectra. The orbital bands are marked with red dashed lines (eccentricity-100 kyr, obliquity-41 kyr, precession-23 kyr and 19 kyr). Clearly variable eccentricity, obliquity and precession variances as well as persistent millennial-scale components are observed for loess Ca/Ti and MMV.



477

478 **Figure. 4** Comparison of a) 35°N summer insolation forcing, b) GHG radiative forcing (black dish

479 line donates the precession band-pass filtering results of ΔRF_{GHG}) and e) ice volume and f) ETP

480 for MMV of Linxia loess Ca/Ti; Wavelet coherence between c) 35°N summer insolation, d) GHG

481 radiative forcing, g) ice volume, h) ETP and MMV of loess Ca/Ti over the past 650 ka. The orbital

482 bands are marked with red dashed lines (eccentricity-100 kyr, obliquity-41 kyr, precession-23 kyr

483 and 19 kyr). The orange color indicates strong correlation for the two time series. The black lines

484 plot coefficients of determination is more than 0.76. The black arrows represent the phrase

485 relationship with rightward, upward and downward arrows indicating in-phase, leading and

486 lagging phrase, respectively. Strong eccentricity, weak obliquity and precession bands ice volume

487 modulation are observed for MMV of loess Ca/Ti. Strong eccentricity and precession bands GHG

488 modulation as well as weak summer insolation forcing are detected for MMV of loess Ca/Ti.

489